Polymer Testing 135 (2024) 108470

Contents lists available at ScienceDirect

Polymer Testing

journal homepage: www.elsevier.com/locate/polytest

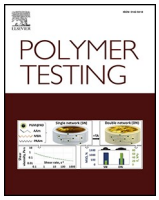

Novel amorphous/crystalline MnO_2 sheet-reinforced rGO/surface-treated BN and epoxy composites with significantly enhanced thermal conductivity and EMI shielding effectiveness

Jihoon Kim [a], Eunsu Jang [a], Jangwoo Cho [a], Peichen Su [c], Jooheon Kim [a,b,*]

[a] Department of Chemical Engineering, Chung-Ang University, 84 Heukseok-ro, Dongjak-gu, Seoul, Republic of Korea
[b] Department of Intelligent Energy and Industry, Graduate School, Chung-Ang University, Seoul 06974, Republic of Korea
[c] School of Mechanical and Aerospace Engineering, Nanyang Technological University, Singapore

ARTICLE INFO

Keywords:
Thermal conductivity
Electromagnetic interference shielding effectiveness
Hybrid sheet
Hydrogen bonding
MnO_2 sheet

ABSTRACT

Rapid technological advancements have significantly increased the amount of heat generated by electronic devices. In addition to heat, electronic devices can malfunction because of electromagnetic (EM) waves. Therefore, research is required on heat management materials with high electromagnetic interference shielding effectiveness (EMI SE). In this study, composites were prepared using reduced graphene oxide (rGO) and boron nitride (BN) as fillers and epoxy as the matrix. To improve dispersion, BN was surface-treated with hydroxyl groups (BN–OH). We have produced amorphous/crystalline novel MnO_2 sheets that exhibited strong interactions with the hydroxyl groups, forming hydrogen bonds with the fillers and matrix. We utilized the strong hydrogen bonding within the amorphous/crystalline domains of novel MnO_2 sheets. The novel MnO_2 sheets significantly enhanced interfacial compatibility between rGO/BN–OH fillers and the epoxy matrix. rGO and BN-OH fillers were able to uniformly disperse on the MnO_2 sheets. The uniform dispersion of fillers contributed to the formation of efficient pathways for heat and electrical conduction, resulting in high electrical conductivity (16.12 S/cm), EMI SE (83.17 dB), and through-plane thermal conductivity (5.84 W/m•K). Owing to the strong interactions between the rGO/BN–OH, MnO_2, and Epoxy, the tensile strength improved to 78.36 MPa.

1. Introduction

The amount of heat generated by electronic devices increases with their advancement. Failure to manage heat properly can negatively impact the operation of electronic devices [1,2]. Therefore, the development of heat management materials is important [3–6]. In addition to heat, electromagnetic interference (EMI) can have detrimental effects on electronic devices [7–10]. Electromagnetic (EM) waves undergo reflection and absorption, ultimately converting to thermal energy [11–14]. Therefore, materials with good thermal management and electromagnetic interference shielding effectiveness (EMI SE) are needed [15–17].

Research has been conducted on polymer-based composites to develop such materials [18–21]. Polymers have been widely used because of their lightweight, excellent processability, corrosion resistance, and low cost [22–26]. However, owing to the low electrical and thermal conductivities of polymers, their thermal management and EMI SE performance are not favorable. Adding fillers with high thermal conductivity to the polymer matrix can enhance the thermal conductivity. Such fillers include alumina [27–31], graphene [32–34], boron nitride (BN) [35–39], carbon nanotube [40–42], aluminum nitride [43–45], and reduced graphene oxide (rGO) [46–48]. BN has a high aspect ratio and corrosion resistance, and low dielectric constant [49]. In addition, rGO has a low thermal expansion coefficient, superior mechanical properties, low density, and high thermal conductivity [50]. The excellent electrical conductivity and high aspect ratio of rGO contribute to the enhancement of the EMI SE.

In this study, BN and rGO were selected as the hybrid fillers. Thermally conductive polymer composites were prepared by utilizing the high thermal conductivities of BN and rGO. Thanks to the high electrical conductivity of rGO, the composite has high EMI SE. Novel MnO_2 sheets were introduced to enhance the dispersion of BN and rGO. The amorphous/crystalline domain of MnO_2 sheets exhibited strong compatibility with hydroxyl functional groups [51], resulting in high compatibility

* Corresponding author. Department of Chemical Engineering, Chung-Ang University, 84 Heukseok-ro, Dongjak-gu, Seoul, Republic of Korea.
E-mail address: jooheonkim@cau.ac.kr (J. Kim).

https://doi.org/10.1016/j.polymertesting.2024.108470
Received 9 January 2024; Received in revised form 28 April 2024; Accepted 28 May 2024
Available online 29 May 2024

with oxygen functional groups of rGO. Despite the reduction in the number of oxygen functional groups, rGO retained its hydroxyl groups and maintained high compatibility with MnO_2. Hydroxyl functional groups (BN–OH) were introduced to enhance the compatibility of BN. Taking this into consideration, epoxy, a hydroxyl-group-rich polymer, was selected as the matrix. Epoxy is widely used in various industries owing to its numerous outstanding properties, including high chemical stability, good mechanical properties, good adhesion, and processability [52]. Epoxy was selected as the polymer matrix to exploit these benefits.

There has been considerable research on polymer composites using rGO and BN as fillers. Cho et al. fabricated epoxy composites using rGO/BN hybrid fillers. They achieved a thermal conductivity of up to 4.12 W/m•K through the hot-press method [53]. Muratov et al. fabricated polypropylene composites using BN and rGO. Both the thermal conductivity (0.867 W/m•K) and strength (50.6 MPa) of the composites improved [54]. Hong et al. prepared thermoplastic polyurethane/rGO/BN composites with high thermal conductivity (6.55 W/m•K) and EMI SE (69 dB) using melt-mixing and hot-pressing [55]. Zhang et al. produced epoxy/BN/rGO composites with a thermal conductivity of 1.07 W/m•K and tensile strength of 53.3 MPa. They utilized the surface functionalization method on BN [56]. However, there is a lack of research that simultaneously enhances the thermal conductivity, EMI SE, and tensile strength of composites. Furthermore, there were limitations in improving the compatibility between rGO, BN, and polymer.

The interfacial compatibility between the matrix and filler is crucial for fabricating composites. The components of the composites must be uniformly dispersed for outstanding performance of the composite [57–60]. In this study, both matrix and filler contained hydroxyl groups and also exhibited hydrophilicity. Therefore, they can form hydrogen bonds, thereby enhancing interfacial compatibility. In particular, amorphous/crystalline regions of novel MnO_2 sheets exhibit strong compatibility with hydroxyl groups, which significantly improves the dispersion of the filler. In the case of rGO, a decrease in the number of OH groups decreased the compatibility with BN–OH. Owing to the strong compatibility of the MnO_2 sheets with the OH groups, a uniform dispersion of both rGO and BN–OH was achieved on the MnO_2 sheets (rGO/BN–OH/MnO_2). Hydroxylated BN and rGO formed a continuous pathway, significantly increasing the thermal and electrical conductivities. Because of the uniform dispersion of the fillers and sheet structures, the EMI SE and mechanical properties were also enhanced.

The composite exhibited high heat dissipation ability and EMI SE. The mechanical properties were also enhanced, demonstrating the feasibility of practical applications. The rGO/BN– OH/MnO_2/epoxy composites showed maximum electrical conductivity of 16.12 S/cm and through-plane thermal conductivity of 5.84 W/m•K at 50 wt% filler content. The tensile strength and elongation at break were enhanced by up to 78.36 MPa and 9.71 %, respectively, at 30 wt% filler content. Based on these outstanding performances, we anticipate that the composite prepared in this study will significantly enhance the heat dissipation ability and EMI SE of electronic devices.

2. Experimental

2.1. Materials

The information about materials can be found in the supplementary information.

2.2. Preparation of rGO/BN–OH hybrid fillers

The detailed experimental procedure is available in the supplementary information.

2.3. Preparation of novel MnO_2 sheets and rGO/BN–OH/MnO_2 hybrid fillers

The detailed experimental procedure is available in the supplementary information.

2.4. Fabrication of composites

The detailed experimental procedure is available in the supplementary information.

2.5. Characterization

Characterization information can be found in the supplementary information.

3. Results and discussion

3.1. Composites fabrication process

Fig. 1 depicts the fabrication processes of the fillers and composites. The detailed procedure is explained in the Supplementary Information.

3.2. Fillers characterization

Fig. 2 shows the morphologies of the fillers. Fig. 2(a) depicts the raw GO/BN–OH fillers, showing the GO and BN–OH sheets. The good compatibility between the two fillers resulted in good dispersion. The hydrophilic functional groups of BN–OH and GO improved the interfacial compatibility. By contrast, rGO/BN–OH (Fig. 2(b)) exhibited reduced compatibility. This was attributed to the reduction in the number of oxygen functional groups as the GO was reduced. The presence of voids and defects spaces is confirmed. Novel MnO_2 sheets were introduced to enhance the compatibility between the rGO and BN–OH (Fig. 2(c)). The amorphous/crystalline MnO_2 sheets exhibited strong compatibility with hydroxyl groups [51], facilitating the effective dispersion of rGO and BN–OH. This is because hydrogen bonds were formed between the fillers. Despite the reduced number of oxygen functional groups on rGO, the presence of hydroxyl groups allowed MnO_2 sheets to act as a bridge between rGO and BN–OH. Therefore, rGO/BN–OH/MnO_2 exhibited improved interfacial compatibility. The MnO_2 sheets improved the dispersibility of the BN–OH and rGO sheets. Therefore, rGO/BN–OH/MnO_2 exhibited the most uniform surface among the fillers. The FE-SEM images of MnO_2 sheets are presented in Fig. S3.

Fig. 3 demonstrates the FTIR spectra of the fillers. Unlike raw BN, BN–OH exhibited a broad peak at approximately 3200 cm^{-1}. This was attributed to the stretching vibration of B–OH. A comparison of the raw BN and BN–OH can be seen in Fig. S4. Fig. 3(a) depicts that raw GO/BN–OH exhibited peaks corresponding to the stretching vibrations of O–H (3200 cm^{-1}), C═O (1715 cm^{-1}), C═C (1550 cm^{-1}), and C–O–C (1050 cm^{-1}); these peaks are associated with GO. Peaks were also observed at 1370 and 850 cm^{-1}, corresponding to the in-plane stretching of the B–N bond and the out-of-plane bending of B–N–B, respectively; these peaks correspond to BN. This indicated the successful preparation of the raw GO/BN–OH filler. Fig. 3(b) is the spectrum of rGO/BN–OH. After the reduction of GO, the peaks associated with oxygen functional groups weakened or disappeared. In particular, the C–O–C peak disappeared completely. However, the broad peak at approximately 3200 cm^{-1} (corresponding to O–H stretching vibrations) still persisted in rGO. The increased intensity of the peaks in rGO/BN–OH is attributed to the addition of the hydroxyl groups of BN–OH. The peak at 1588 cm^{-1} is due to the stretching vibrations of aromatic C═C bonds. The peak at 1317 cm^{-1} corresponds to the wagging vibration of CH_2 groups. A peak at 775 cm^{-1} was also observed due to C–H bending vibrations. All peaks related to BN were observed. This confirms

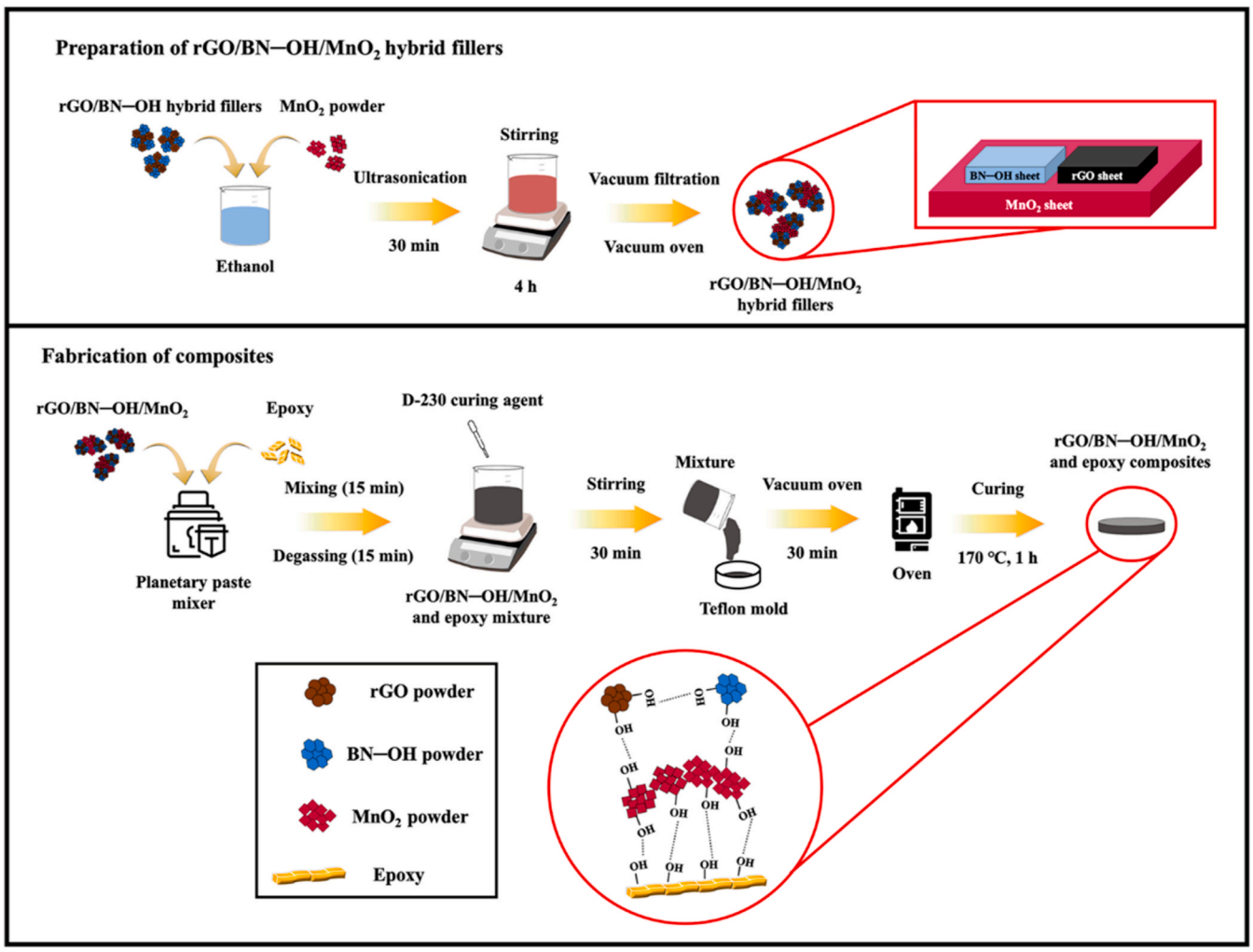

Fig. 1. Illustrations of the preparation process of fillers and composites.

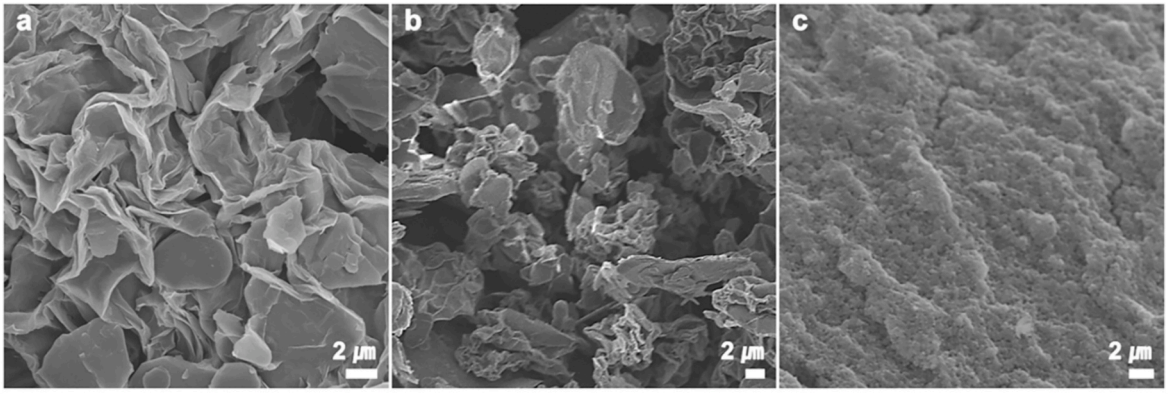

Fig. 2. Morphology of (a) raw GO/BN–OH, (b) rGO/BN–OH, and (c) rGO/BN–OH/MnO_2 fillers.

the successful preparation of rGO/BN–OH. Fig. 3(c) shows the spectrum of rGO/BN–OH/MnO_2. The broad peak at 3420 cm^{-1} is attributed to the stretching vibration of hydroxyl groups. The peaks observed at 1632, 1378, and 1027 cm^{-1} correspond to the bending vibrations of Mn–OH bonds. Additionally, all peaks related to BN and rGO were observed. This confirmed the successful incorporation of MnO_2 sheets into rGO/BN–OH.

An XPS analysis was conducted to verify the chemical bonding of the fillers. The survey spectra for all the fillers are provided in Fig. S5. The elemental composition was consistent with that provided in a previous report [61]. Fig. 4(a) shows the XPS spectra of BN–OH. Peaks are observed at 190.7 eV (B–N) and 192.3 eV (B–O) in the B1s spectrum. The presence of peaks related to B–O indicates that the hydroxylation of BN proceeded well. Peaks were observed only at 398.3 eV in the N1s spectrum, which are attributed to the B–N bonds. Two peaks appeared at 532.8 eV (O–H) and 531.7 eV (B–O) in the O1s spectrum. This also

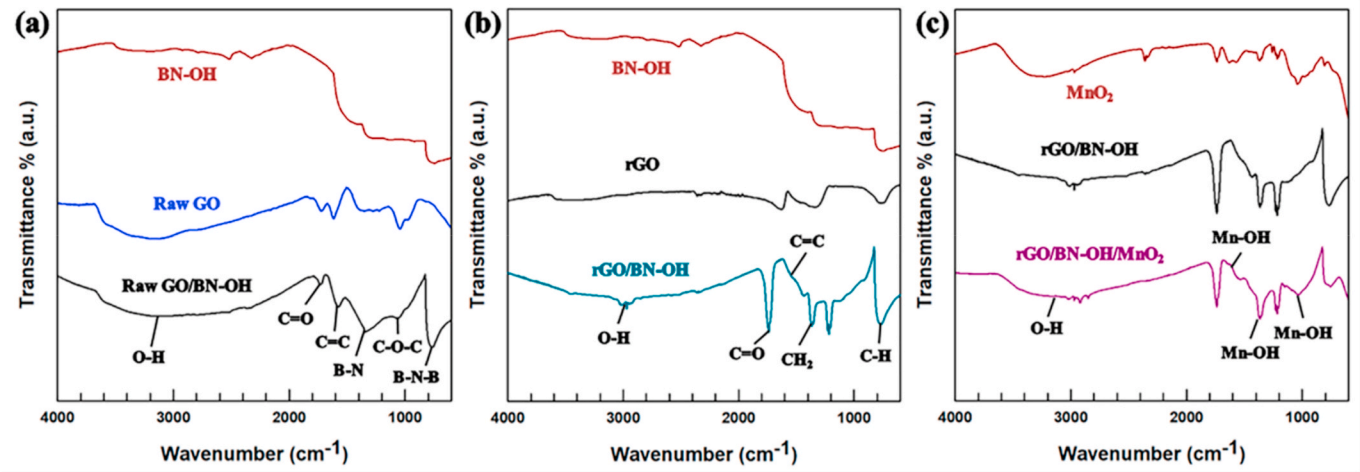

Fig. 3. FT-IR spectra of (a) raw GO/BN–OH, (b) rGO/BN–OH, and (c) rGO/BN–OH/MnO_2 fillers.

indicates the introduction of hydroxyl groups to BN. For comparison, XPS analysis of Raw BN was also conducted (Fig. S6). Fig. 4(b) exhibits the spectra of raw GO/BN–OH. The C1s spectrum exhibits peaks corresponding to graphitic carbon C═C (284.4 eV), C–C (285.0 eV), C–N (285.6 eV), C–O (286.8 eV), and C═O (289.2 eV) bonds. The C–N peak confirms the interaction between GO and BN–OH. The B1s spectrum exhibits peaks associated with B–N (190.3 eV), B–C (190.4 eV), and B–O (191.2 eV). The newly observed B–C and B–O peaks further confirm the interaction between GO and BN–OH. Peaks corresponding to B–N (397.6 eV) and C–N (397.9 eV) are observed in the N1s spectrum. The appearance of the C–N peak indicated the successful fabrication of the raw GO/BN–OH hybrid filler. Fig. 4(c) shows XPS spectra of rGO/BN–OH filler. All the peaks observed in the C1s spectrum of raw GO/BN–OH were present. Owing to the reduction of GO, the intensity of the peaks related to the oxygen functional groups decreased. Peaks similar to those of raw GO/BN–OH were observed in the B1s spectrum. The intensity of the oxygen-containing B–O peak decreased owing to the reduction. No significant changes were observed in the peaks of the N1s spectrum. The presence of C–N, B–C, and B–O bonds indicated the successful preparation of rGO/BN–OH hybrid. Fig. 4(d) shows the spectra of rGO/BN–OH/MnO_2 filler. Mn2p spectrum exhibited peaks at 642.0 eV ($Mn2p_{3/2}$) and 653.3 eV ($Mn2p_{1/2}$). After deconvolution, $Mn2p_{3/2}$ exhibited peaks at 642.0 eV (Mn^{3+}) and 642.4 eV (Mn^{4+}). $Mn2p_{1/2}$ displayed two peaks at 652.7 and 653.7 eV. This was consistent with the findings of a previous research [62]. In the O1s spectrum, peaks were observed at 529.4 eV (Mn–O–Mn) and 531.1 eV (Mn–O–H). The presence of Mn-containing functional groups confirmed the successful incorporation of MnO_2.

Fig. 5(a) presents the XRD patterns of the fillers. For raw GO/BN–OH, a strong peak of GO was observed at $2\theta = 10.3°$. The peaks of BN and GO merged into a single peak at $2\theta = 26.5°$ and 41.7°. The peaks at $2\theta =$ 43.7°, 50.1°, 55.1°, and 76.5° correspond to BN. In the case of rGO/BN–OH, changes were observed in the intensity of the peak owing to the reduction of GO. The (001) peak intensity at $2\theta = 10.3°$ decreased and the peak intensity at $2\theta = 26.3°$ increased further. This was attributed to the reduction in the oxygen content of rGO and graphitization. The peak intensity at $2\theta = 41.7°$ decreased because the reduction of GO decreased the intensity of the (100) peak. Similar to raw GO/BN–OH, the merged peaks (26.3° and 41.7°) still appeared. This indicated the presence of interactions between fillers. The peaks related to BN are consistent. For rGO/BN–OH/MnO_2, new peaks corresponding to MnO_2 emerged. These peaks correspond to 12.7°, 28.9°, 36.7°, 41.9°, 52.8°, 56.4°, and 65.4. No changes are observed in the peaks corresponding to BN and rGO. The intensity of the peaks related to MnO_2 was weaker than those of BN and rGO because the BN and rGO sheets covered the MnO_2 sheets. These observations confirmed the successful formation of the rGO/BN–OH/MnO_2 hybrid filler.

Fig. 5(b) exhibits the TGA curves of the fillers. Both BN and rGO exhibited high thermal stabilities, rGO/BN–OH exhibited superior thermal stability. There was a slight mass loss at approximately 130 °C, which was attributed to the decomposition of the hydroxyl groups in BN–OH. The gradual decrease observed after 130 °C is due to the decomposition of oxygen-containing functional groups remaining in rGO; the total mass loss was 4.92 %. Furthermore, rGO/BN–OH/MnO_2 exhibited a greater mass loss than rGO/BN–OH (32.84 %). The mass loss at approximately 100 °C is due to the removal of hydroxyl groups and adsorbed water. This reduction continued up to 200 °C. Between 200 and 400 °C, a mass loss is observed due to the further decomposition of functional groups, such as epoxy and hydroxyl groups, that remain in the rGO. The mass loss observed after 550 °C is attributed to the decomposition of Mn–O bonds. These observations confirm the successful incorporation of MnO_2 into rGO/BN–OH. Raw GO/BN–OH exhibited the lowest thermal stability. The total mass loss was 41.51 %, which was the highest among all the fillers. The mass loss observed below 100 °C is attributed to the evaporation of water molecules. The weight reduction between 100 and 400 °C is due to the removal of hydroxyl groups in BN–OH and oxygen-containing functional groups of GO. After 400 °C, a significant weight loss is observed due to the further removal of oxygen-containing functional groups that remain in GO. These differences confirmed the successful preparation of the fillers.

3.3. Composites morphology

Fig. 6 demonstrates the morphologies of the epoxy matrix and the composites. Fig. 6(a) shows an image of the epoxy matrix. It exhibits a smooth surface compared with that of the composites. Fig. 6(b) depicts the appearance of the composite with the addition of raw GO/BN–OH fillers. Compared to the epoxy matrix, the presence of many sheets (rGO, BN) is evident. Although some smooth areas were present on the surface, there were regions where the sheets were not evenly dispersed. Although hydroxylation of BN improved its compatibility with GO, it did not significantly enhance its dispersibility. Fig. 6(c) shows the morphology of the rGO/BN–OH/epoxy composite. After the reduction of GO, its hydrophilicity decreases, reducing the interfacial compatibility with BN–OH. Consequently, defects, cracks, and agglomerations occurred. These defects cause phonon scattering, which adversely affects phonon transport and ultimately reduces thermal conductivity. The introduction of the amorphous/crystalline MnO_2 sheets significantly improved the dispersibility. Fig. 6(d) depicts the morphology of rGO/BN–OH/MnO_2/epoxy composites. No defects or agglomerations are

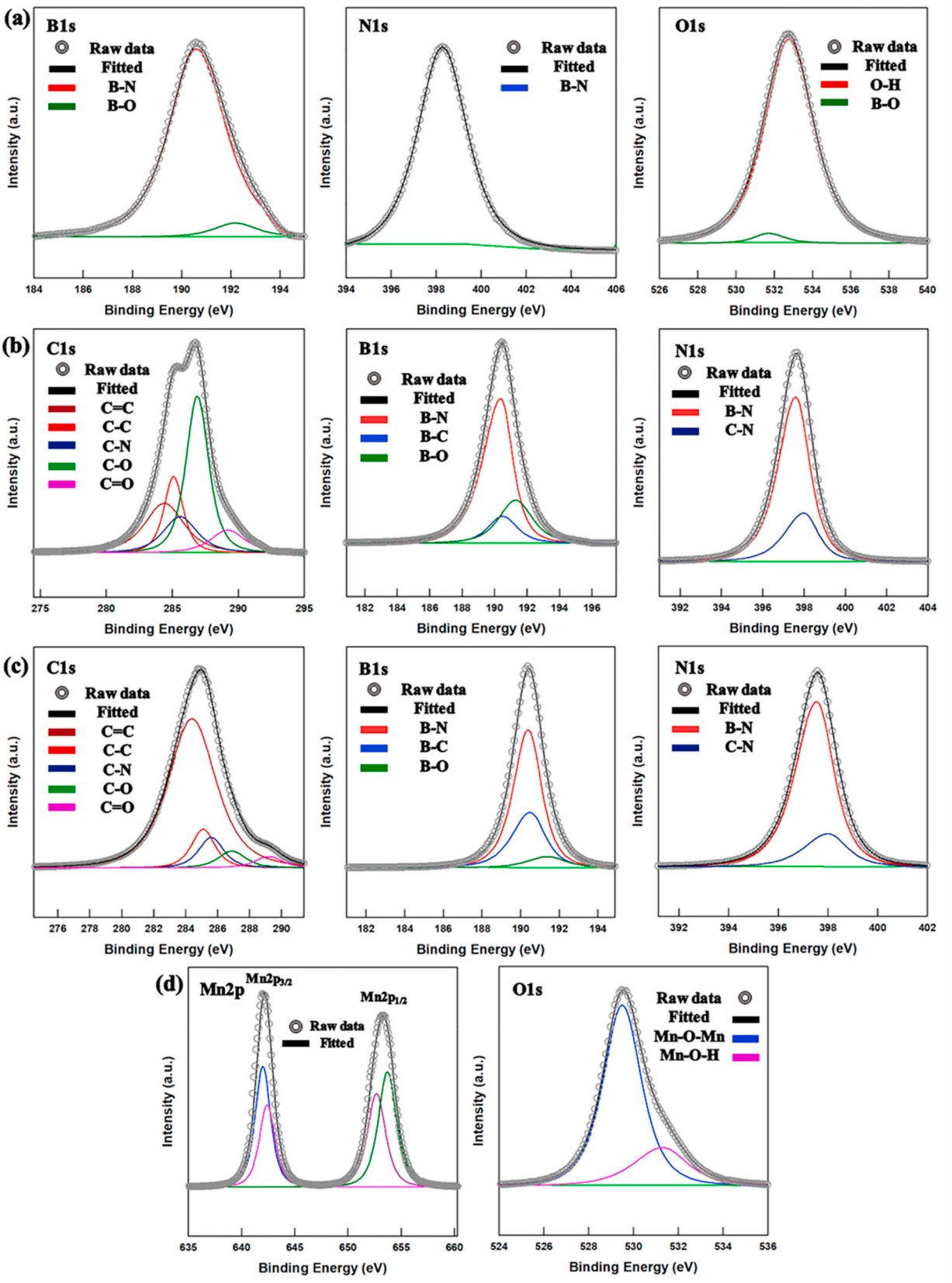

Fig. 4. XPS spectra of (a) BN–OH, (b) raw GO/BN–OH, (c) rGO/BN–OH, and (d) rGO/BN–OH/MnO_2 fillers.

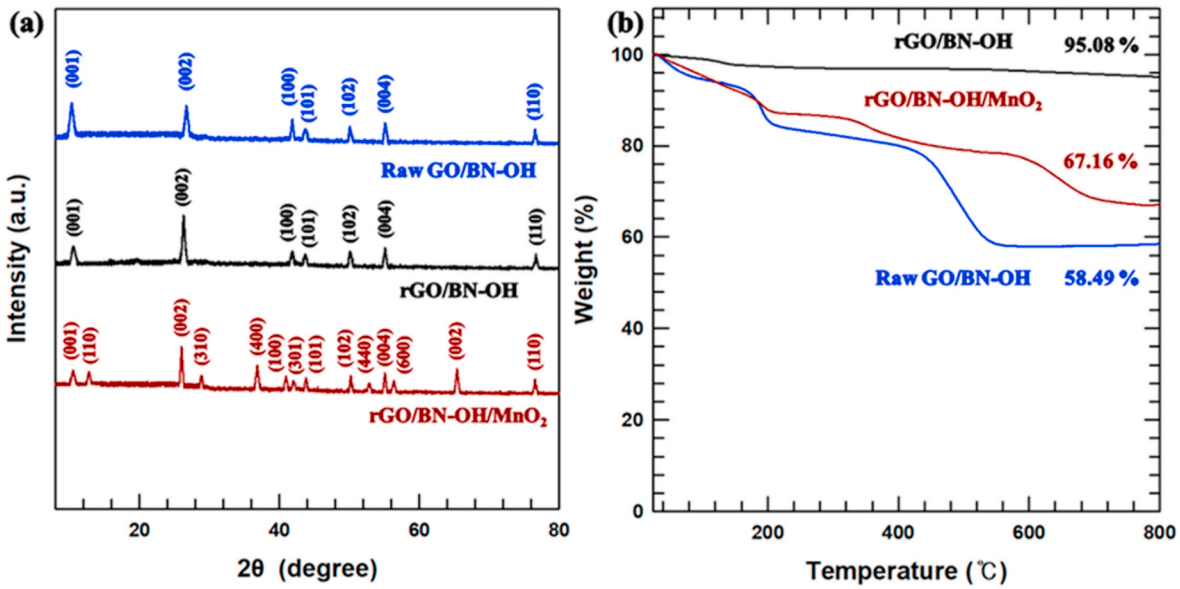

Fig. 5. (a) XRD pattern and (b) TGA graph of the various fillers.

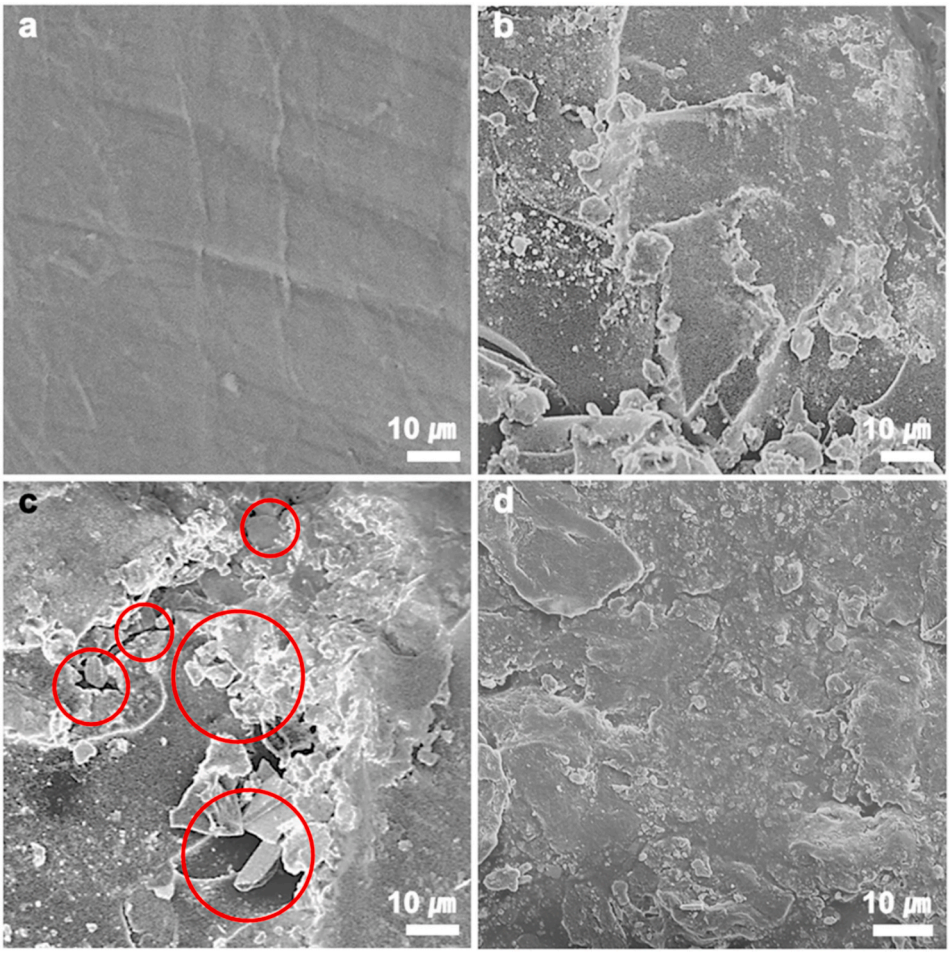

Fig. 6. Morphologies of cross-sectional of (a) epoxy matrix, (b) raw GO/BN–OH/epoxy, (c) rGO/BN–OH/epoxy, and (d) rGO/BN–OH/MnO_2/epoxy.

observed. It exhibited the smoothest surface among all the composites. The amorphous/crystalline region of MnO_2 sheets exhibited strong compatibility with hydroxyl groups, enabling it to form hydrogen bonds with both rGO and BN–OH. This improved dispersibility can be attributed to the MnO_2 sheets, which enhanced the compatibility of the rGO and BN–OH sheets. Furthermore, MnO_2 sheets form hydrogen bonds with the epoxy matrix. MnO_2 served as a link between the rGO/BN–OH and the epoxy. Hence, the amorphous/crystalline novel MnO_2

sheets enhanced not only the interfacial adhesion between the fillers but also that between the fillers and the matrix.

3.4. Properties of composites

F ig. 7(a) and (b) show the electrical conductivities of the composites. The raw GO/BN–OH/epoxy composite did not exhibit electrical conduction properties. Both raw GO and BN–OH are electrically insulating and exhibit low compatibility. Thus, raw GO/BN–OH/epoxy exhibited electrical insulation regardless of the filler content. As GO was reduced, the number of oxygen functional groups decreased, reducing the number of defects. The restoration of sp^2 hybridized carbon and π-conjugated structures enhanced electron transfer. Consequently, the rGO/BN-OH/epoxy composites have high electrical conductivity. Electrical conductivity increased with increasing filler content. Both composites exhibited the most significant enhancement in the electrical conductivity at 30 wt%. This is because filler content exceeded the percolation threshold, resulting in the formation of a continuous electrical conduction pathway. The electrical conductivity of the rGO/BN–OH/MnO_2/epoxy was higher than that of the rGO/BN–OH/epoxy. Novel MnO_2 sheets improved dispersion, resulting in the formation of more effective electrical conduction pathways. The interfacial resistance decreased by the enhanced interfacial compatibility. These positive effects of MnO_2 increased the electrical conductivity. Table S1 lists the electrical conductivity and resistivity of the composites. To verify the effectiveness of BN surface treatment, we measured the electrical conductivity of rGO/Raw BN/epoxy and rGO/Raw BN/MnO_2/epoxy composites (Table S2). Due to the poor compatibility between raw BN and rGO, the electrical conductivity decreased. The percolation threshold was similarly observed between 20 and 30 wt%. The rate of increase in electrical conductivity also decreased. This is because the reduced interfacial compatibility prevented the effective formation of electrical conduction pathways. After the addition of MnO_2 sheets, the electrical conductivity significantly improved. This is because the MnO_2 sheets complemented the weak interaction between rGO and raw BN. These results confirm the reinforcing effect of surface treatment of BN and MnO_2 sheets.

F ig. 7(c) and (d) present the EMI SE values of the composites measured in the X band range of 8.2–12.4 GHz. The EMI SE values of the composites were high owing to their high electrical conductivities. The electrically insulated raw GO/BN–OH/epoxy exhibited poor EMI SE performance below 20 dB, which is the minimum threshold required for practical use. As the filler content increased, the EMI SE improved, with the most significant increase observed at 30 wt%. An increase in the filler content increased the probability of encountering incident EM waves. Consequently, EM wave reflections occurred more frequently. The significant improvement in electrical conductivity due to the formation of electrical pathways leads to a substantial increase in the Ohmic loss. The rGO/BN–OH/MnO_2/epoxy exhibited superior EMI SE performance compared to that of rGO/BN–OH/epoxy because of the reinforcing effect of MnO_2. The high electrical conductivity of the composites increased the absorption and reflection losses, resulting in enhanced EMI SE performance. Fig. 7(e) and (f) demonstrate the total EMI SE (SE_T), EMI SE by absorption (SE_A), and EMI SE by reflection (SE_R). The SE_A was significantly larger than the SE_R for all composites. This is because rGO can effectively absorb EM waves [63]. Values for SE_T, SE_A, and SE_R are summarized in Table S3. We also measured the SE_R, SE_A, and SE_T values of the rGO/Raw BN/epoxy and rGO/Raw BN/MnO_2/epoxy composites (Table S4). Because BN is electrically insulating, it does not directly impact the EMI SE. However, the EMI SE of composites containing Raw BN and BN-OH differed. This is because the reduced interfacial compatibility between rGO and raw BN hindered the formation of electrical conduction pathways by rGO. This led to aggregation among rGO, resulting in decreased performance. This signifies that raw BN indirectly impacted the EMI SE. After the addition of MnO_2 sheets, the EMI SE improved. This confirms the reinforcing effect of MnO_2 sheets. Fig. 8 shows the EMI SE mechanisms of the composites. The highly conductive rGO sheets effectively reflect the incident EM waves owing to their large aspect ratio. The impedance mismatch between air and the composites caused reflections. The EM waves were either reflected or absorbed. Because the composites developed in this study have very low reflection losses, they can effectively reduce the re-reflection, which reduces secondary contamination. Multiple reflections and interfacial polarizations occur because of the various sheet structures and interfaces. As reflection occurred, the EM waves weakened and were eventually absorbed by the rGO sheets. The EM waves were attenuated by continuously repeating this process. The EM waves were converted into thermal energy and then emitted.

Fig. 9(a) is a graph depicting the through-plane thermal conductivities of the composites as a function of filler content. The thermal conductivity values of the composites are provided in Table S5. Fig. 9(b) shows the thermal conductivity values predicted using the Agari–Uno model. The experimental values were consistent with those obtained from the model, confirming the accuracy of the predictions. A detailed explanation of the Agari–Uno modeling process can be found in the extended discussion section of the Supporting Information. The thermal conductivity increased with increasing filler content, with the most significant increase observed at 30 wt%. Similar to electrical conductivity, the filler created thermal conduction pathways by surpassing the percolation threshold. The raw GO/BN–OH/epoxy composites showed the lowest thermal conductivity among the composites, attributed to the low thermal conductivity of GO. Furthermore, rGO shows significantly improved thermal conductivity owing to the reduction in oxygen functional groups, which enhanced the heat transfer efficiency. While the interfacial compatibility between rGO and BN–OH decreased, the influence of rGO was dominant, leading to a high thermal conductivity in the rGO/BN–OH/epoxy composites. The thermal conductivity values of the rGO/Raw BN/epoxy and rGO/Raw BN/MnO_2/epoxy composites were also measured (Table S6). The thermal conductivity values of these composites were lower than those of the rGO/BN-OH/epoxy and rGO/BN-OH/MnO_2/epoxy composites. This is because the decreased interfacial compatibility between rGO and raw BN led to an increase in interfacial thermal resistance. This resulted in phonon scattering, negatively impacting phonon transport. After the addition of MnO_2 sheets, the thermal conductivity improved. This is because MnO_2 sheets enhanced interfacial adhesion between rGO and raw BN sheets. This allowed us to recognize the contribution of BN surface treatment and MnO_2 sheets to the improvement in thermal conductivity. Fig. 9(c) shows a schematic of the heat transfer mechanism of the rGO/BN–OH/MnO_2/epoxy composite. The introduction of MnO_2 sheets further enhanced the thermal conductivity. The rGO and BN–OH sheets are evenly dispersed on the MnO_2 sheets. The reduced hydrophilicity of rGO results in its poor compatibility with epoxy. The MnO_2 sheets enhanced the interfacial adhesion by serving as a connecting agent. Owing to its strong compatibility with hydroxyl groups, MnO_2 forms hydrogen bonds with rGO, BN–OH, and epoxy. The improved interfacial compatibility of the fillers and matrix–fillers reduced the interfacial thermal resistance. The rGO and BN sheets created continuous pathways on the MnO_2 sheets, which reduces the phonon scattering, leading to efficient phonon transport. Free electrons in the rGO also contribute to heat conduction. Hence, the rGO/BN–OH/MnO_2/epoxy composite exhibits excellent thermal dissipation performance.

Tensile strength and strain were measured to assess the mechanical properties of the composites. The epoxy matrix exhibited a maximum tensile strength of 30.64 MPa at a strain of 2.9 %. After the addition of the rGO/BN–OH/MnO_2 hybrid filler (Fig. 10(a)), both strength and strain significantly improved. The results for the tensile strength and strain are listed in Table S7. At the filler content of 30 wt%, the tensile strength and strain were the highest, measuring 78.36 MPa and 9.71 %, respectively. The enhanced interfacial compatibility between the fillers is mainly attributed to the hydrogen bonds formed between the fillers. The significant improvement in the interfacial adhesion between the

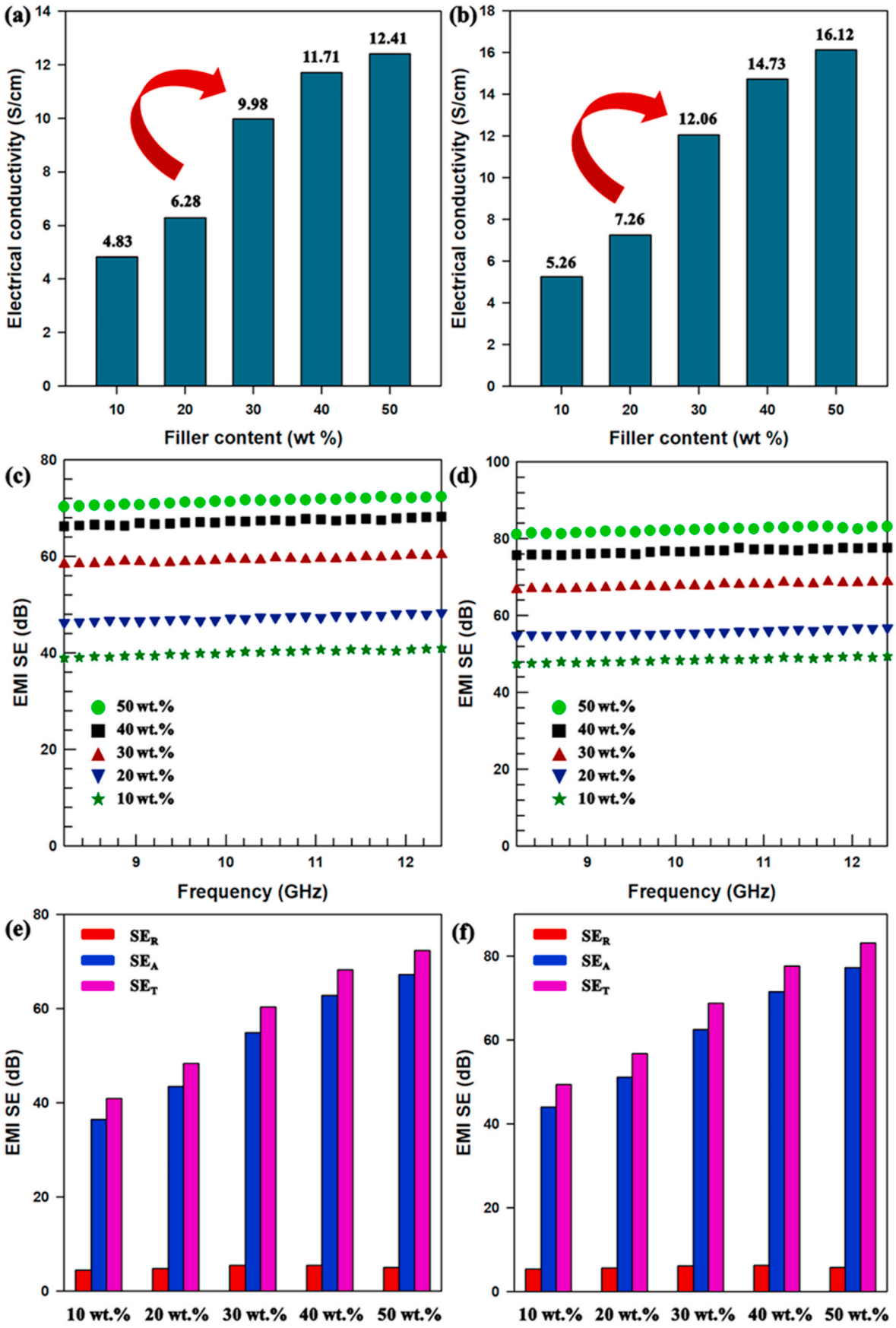

Fig. 7. Electrical conductivities of (a) rGO/BN–OH/epoxy and (b) rGO/BN–OH/MnO_2/epoxy. Total EMI SE of (c) rGO/BN–OH/epoxy and (d) rGO/BN–OH/MnO_2/epoxy. SE_T, SE_A, and SE_R values of (e) rGO/BN–OH/epoxy and (f) rGO/BN–OH/MnO_2/epoxy.

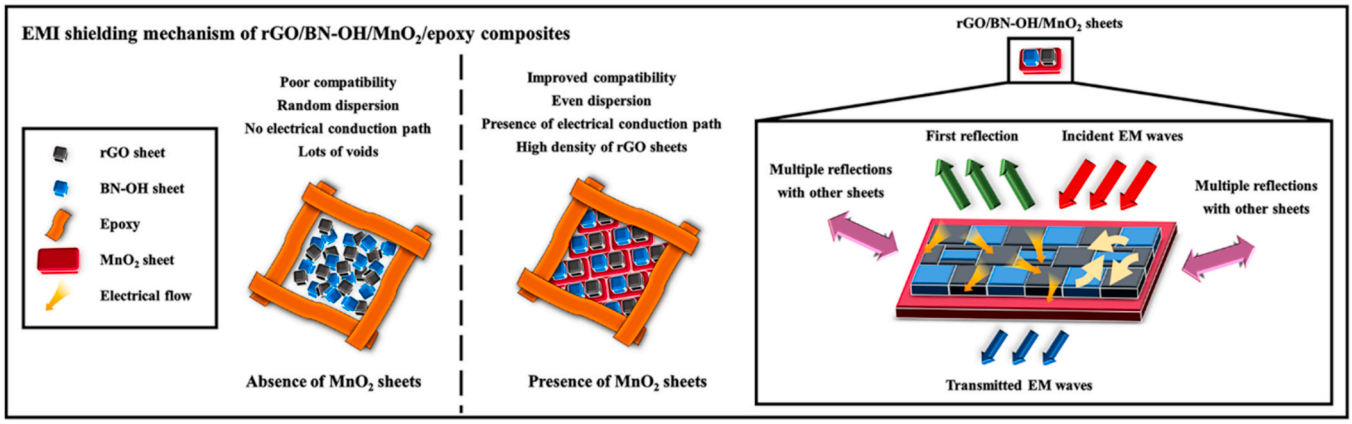

Fig. 8. EMI shielding mechanism of rGO/BN–OH/MnO_2/epoxy composite.

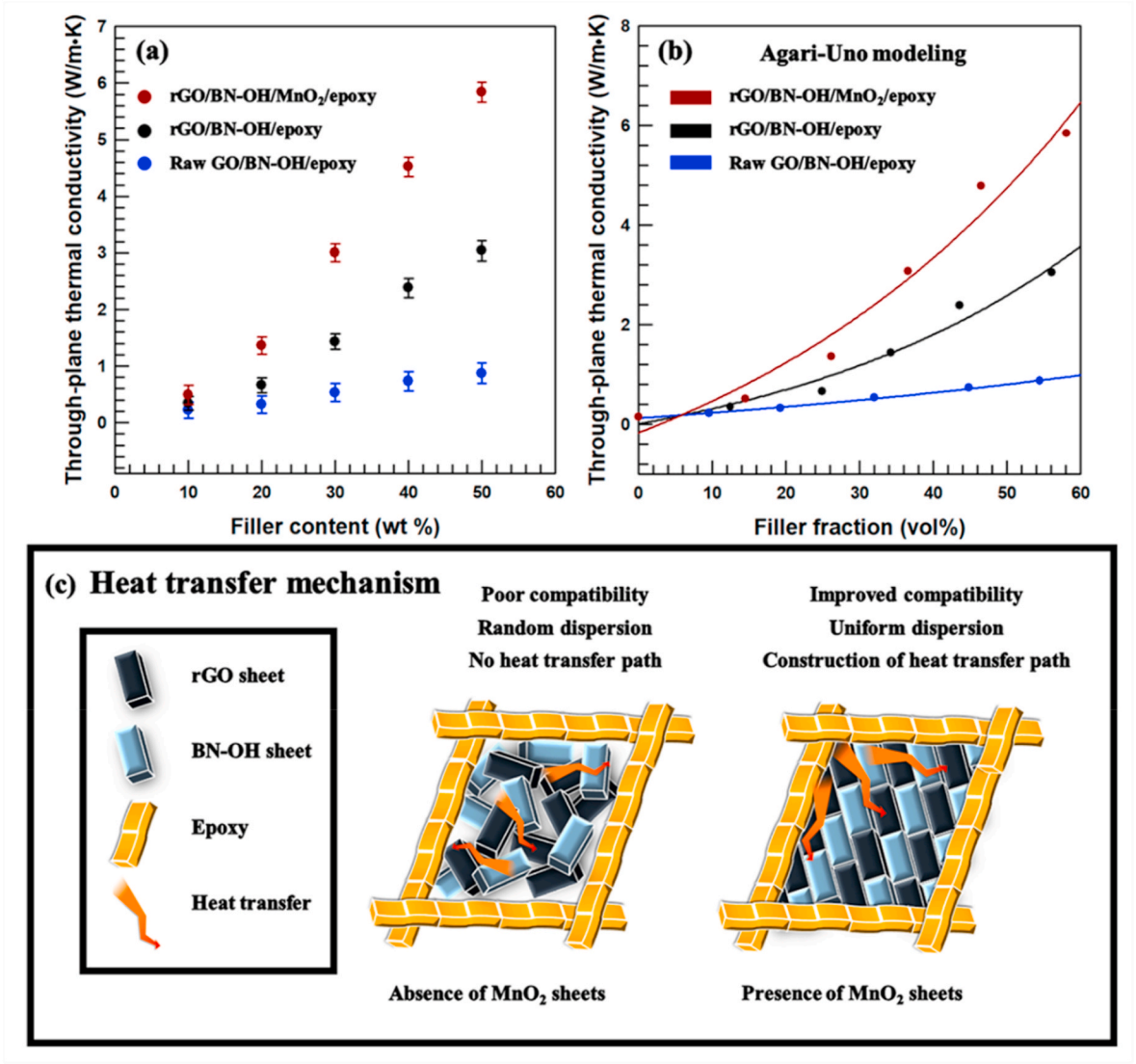

Fig. 9. (a) Through-plane thermal conductivity values. (b) Prediction of thermal conductivity using Agari–Uno modeling. (c) Heat transport mechanism of rGO/BN–OH/MnO_2/epoxy composites.

epoxy matrix and fillers can be attributed to the hydrogen bonds and cross-linking between them. The even dispersion of the fillers contributes to an even distribution of stress within the composites, which in turn improves their mechanical properties. However, when the filler content increased further, the mechanical properties deteriorated. This is because the aggregation of the fillers led to the generation of stress

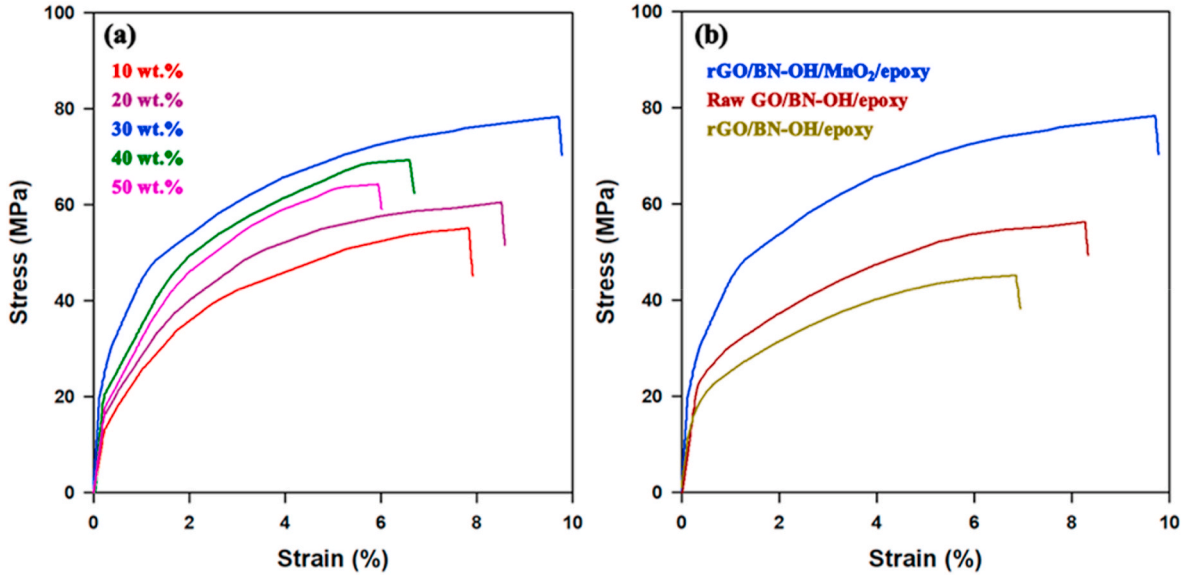

Fig. 10. (a) Tensile stress curve of rGO/BN–OH/MnO_2/epoxy composites. (b) Stress–strain curve of raw GO/BN–OH/epoxy, rGO/BN–OH/epoxy, and rGO/BN–3OH/MnO_2/epoxy composites.

concentration points. The uneven distribution of stress hindered the effective stress transfer, negatively affecting the tensile strength. The tensile strengths and strains of the composites are presented in Fig. 10 (b). The mechanical properties of the composites are listed in Table S8. The rGO/BN–OH/epoxy composite exhibited the lowest performance due to the poor compatibility between different fillers, and between the fillers and matrix. Raw GO/BN–OH/epoxy showed improved mechanical properties compared to rGO/BN–OH/epoxy. The hydrophilic GO and BN–OH exhibited strong interactions owing to hydrogen bonding. Interfacial adhesion was also strengthened through hydrogen bonding with the epoxy. We evaluated the mechanical properties when BN surface treatment was not applied (Table S9). Both tensile strength and strain decreased compared to composites containing surface-treated BN. This is because the interfacial interaction between fillers was reduced, leading to a decrease in interfacial adhesion. The tensile strength and strain of the composite were the highest when MnO_2 was included. This is because MnO_2 strengthened the interfacial adhesion. The dispersing effect of MnO_2 prevented filler aggregation. The reinforcing effect of MnO_2 was limited due to the absence of hydroxyl functional groups on raw BN. These results suggest that BN-OH and MnO_2 sheets enhance mechanical properties. Thus, the surface treatment of BN enhanced the mechanical properties of the composites. However, surface treatment alone was not sufficient to significantly improve the compatibility. The addition of MnO_2 sheets further improved the mechanical properties of the composites. MnO_2 sheets present between rGO/BN–OH and epoxy significantly improved the compatibility. Furthermore, strong interactions were formed, leading to a significant enhancement in interfacial adhesion. The improved compatibility led to uniform filler dispersion and suppressed the occurrence of stress concentration spots. Owing to uniform stress transfer, rGO/BN–OH/MnO_2/epoxy exhibited the best mechanical properties.

4. Conclusion

In this study, amorphous/crystalline novel MnO_2 sheets were used to enhance interfacial compatibility. The hydroxylation of BN resulted in the formation of hydrogen bonds between rGO and BN–OH, as well as MnO_2 sheets and epoxy, significantly improving the interfacial adhesion. The MnO_2 sheets connected the rGO, BN–OH, and epoxy groups, enhancing their compatibility. Thanks to the enhanced interfacial compatibility, the interfacial thermal resistance decreased; therefore, the composites exhibited a maximum through-plane thermal conductivity of 5.84 W/m•K. Owing to the uniform dispersion of fillers and the excellent electrical conductivity of rGO, electrical flow pathways were established. Consequently, the composites exhibited high electrical conductivity and an EMI SE of up to 83.17 dB. The reinforced filler–filler and filler–matrix interactions enhanced the tensile strength, reaching a maximum of 78.36 MPa. Thus, the fabricated rGO/BN–OH/MnO_2/epoxy composites exhibited excellent heat-dissipation performance and EMI SE. These composites are expected to be useful in devices requiring heat management or EMI shielding.

CRediT authorship contribution statement

Jihoon Kim: Writing – review & editing, Writing – original draft, Methodology, Investigation, Formal analysis, Conceptualization. **Eunsu Jang:** Writing – review & editing, Investigation, Formal analysis, Data curation. **Jangwoo Cho:** Writing – review & editing, Investigation, Formal analysis, Data curation. **Peichen Su:** Visualization, Software, Data curation. **Jooheon Kim:** Validation, Supervision, Resources, Project administration, Funding acquisition.

Declaration of competing interest

The authors declare that they have no known competing financial interests or personal relationships that could have appeared to influence the work reported in this paper.

Data availability

The data that has been used is confidential.

Acknowledgements

This research was supported by the National Research Foundation of Korea (NRF) grant funded by the Korea government (MSIT) (NRF-2022M3H4A1A02076956).

Appendix A. Supplementary data

Supplementary data to this article can be found online at https://doi.org/10.1016/j.polymertesting.2024.108470.

References

[1] W. Huang, R.G. Askin, Reliability analysis of electronic devices with multiple competing failure modes involving performance aging degradation, Qual. Reliab. Eng. Int. 19 (2003) 241–254, https://doi.org/10.1002/qre.524.

[2] C.W. Park, S.K. Kang, H.L. Hernandez, J.A. Kaitz, D.S. Wie, J. Shin, O.P. Lee, N. R. Sottos, J.S. Moore, J.A. Rogers, S.R. White, Thermally Triggered degradation of transient electronic devices, Adv. Mater. 27 (2015) 3783–3788, https://doi.org/10.1002/adma.201501180.

[3] L. Sang, Diamond as the heat spreader for the thermal dissipation of GaN-based electronic devices, Functional Diamond 1 (2021) 174–188, https://doi.org/10.1080/26941112.2021.1980356.

[4] W. Zhang, Q.Q. Kong, Z. Tao, J. Wei, L. Xie, X. Cui, C.M. Chen, 3D thermally cross-linked graphene aerogel–enhanced silicone rubber elastomer as thermal interface material, Adv Mater Interfaces 6 (2019), https://doi.org/10.1002/admi.201900147.

[5] W. Dai, L. Lv, J. Lu, H. Hou, Q. Yan, F.E. Alam, Y. Li, X. Zeng, J. Yu, Q. Wei, X. Xu, J. Wu, N. Jiang, S. Du, R. Sun, J. Xu, C.P. Wong, C. Te Lin, A paper-like inorganic thermal interface material composed of hierarchically structured graphene/silicon carbide nanorods, ACS Nano 13 (2019) 1547–1554, https://doi.org/10.1021/acsnano.8b07337.

[6] Y. Zhang, Y. Yan, J. Guo, T. Lu, J. Liu, J. Zhou, X. Xu, Superior thermal dissipation in graphene electronic device through novel heat path by electron-phonon coupling, ES Energy and Environment 8 (2020) 42–47, https://doi.org/10.30919/esee8c386.

[7] P. Tao, W. Shang, C. Song, Q. Shen, F. Zhang, Z. Luo, N. Yi, D. Zhang, T. Deng, Bioinspired engineering of thermal materials, Adv. Mater. 27 (2015) 428–463, https://doi.org/10.1002/adma.201401449.

[8] M.A. Poothanari, J. Abraham, N. Kalarikkal, S. Thomas, Excellent electromagnetic interference shielding and high electrical conductivity of compatibilized polycarbonate/polypropylene carbon nanotube blend nanocomposites, Ind. Eng. Chem. Res. 57 (2018) 4287–4297, https://doi.org/10.1021/acs.iecr.7b05406.

[9] J. Abraham, M. Arif P, P. Xavier, S. Bose, S.C. George, N. Kalarikkal, S. Thomas, Investigation into dielectric behaviour and electromagnetic interference shielding effectiveness of conducting styrene butadiene rubber composites containing ionic liquid modified MWCNT, Polymer (Guildf) 112 (2017) 102–115, https://doi.org/10.1016/j.polymer.2017.01.078.

[10] M. Wang, X.H. Tang, J.H. Cai, H. Wu, J. Bin Shen, S.Y. Guo, Construction, mechanism and prospective of conductive polymer composites with multiple interfaces for electromagnetic interference shielding: a review, Carbon N Y 177 (2021) 377–402, https://doi.org/10.1016/j.carbon.2021.02.047.

[11] H. Lv, Y. Guo, G. Wu, G. Ji, Y. Zhao, Z.J. Xu, Interface polarization strategy to solve electromagnetic wave interference issue, ACS Appl. Mater. Interfaces 9 (2017) 5660–5668, https://doi.org/10.1021/acsami.6b16223.

[12] Q. Liu, Q. Cao, H. Bi, C. Liang, K. Yuan, W. She, Y. Yang, R. Che, CoNi@SiO2@TiO2 and CoNi@air@TiO2 microspheres with strong wideband microwave absorption, Adv. Mater. 28 (2016) 486–490, https://doi.org/10.1002/adma.201503149.

[13] B. Wen, M. Cao, M. Lu, W. Cao, H. Shi, J. Liu, X. Wang, H. Jin, X. Fang, W. Wang, J. Yuan, Reduced graphene oxides: light-weight and high-efficiency electromagnetic interference shielding at elevated temperatures, Adv. Mater. 26 (2014) 3484–3489, https://doi.org/10.1002/adma.201400108.

[14] H. Lv, G. Ji, H. Zhang, M. Li, Z. Zuo, Y. Zhao, B. Zhang, D. Tang, Y. Du, Co x Fe y @C composites with tunable atomic ratios for excellent electromagnetic absorption properties, Sci. Rep. 5 (2015), https://doi.org/10.1038/srep18249.

[15] H. Fang, H. Guo, Y. Hu, Y. Ren, P.C. Hsu, S.L. Bai, In-situ grown hollow Fe3O4 onto graphene foam nanocomposites with high EMI shielding effectiveness and thermal conductivity, Compos. Sci. Technol. 188 (2020), https://doi.org/10.1016/j.compscitech.2019.107975.

[16] X. Jin, J. Wang, L. Dai, X. Liu, L. Li, Y. Yang, Y. Cao, W. Wang, H. Wu, S. Guo, Flame-retardant poly(vinyl alcohol)/MXene multilayered films with outstanding electromagnetic interference shielding and thermal conductive performances, Chem. Eng. J. 380 (2020), https://doi.org/10.1016/j.cej.2019.122475.

[17] K. Wu, Y. Xue, W. Yang, S. Chai, F. Chen, Q. Fu, Largely enhanced thermal and electrical conductivity via constructing double percolated filler network in polypropylene/expanded graphite – multi-wall carbon nanotubes ternary composites, Compos. Sci. Technol. 130 (2016) 28–35, https://doi.org/10.1016/j.compscitech.2016.04.034.

[18] J. Kim, J. Kim, Pyrolyzed cellulose/rGO aerogel composites via I2 treatment and silane surface functionalization with highly improved through-plane thermal conductivity and EMI shielding effectiveness, J. Mater. Res. Technol. 26 (2023) 2782–2795, https://doi.org/10.1016/j.jmrt.2023.08.083.

[19] Z. Shen, J. Feng, Preparation of thermally conductive polymer composites with good electromagnetic interference shielding efficiency based on natural wood-derived carbon scaffolds, ACS Sustain Chem Eng 7 (2019) 6259–6266, https://doi.org/10.1021/acssuschemeng.8b06661.

[20] B. Wei, L. zhang, S. Yang, Polymer composites with expanded graphite network with superior thermal conductivity and electromagnetic interference shielding performance, Chem. Eng. J. 404 (2021), https://doi.org/10.1016/j.cej.2020.126437.

[21] J. Kim, J. Kim, PBO fiber grafted rGO aerogel/BN/PBO composites with highly improved electromagnetic interference shielding effectiveness and through-plane thermal conductivity, Polym. Test. 129 (2023), https://doi.org/10.1016/j.polymertesting.2023.108282.

[22] L. Wang, H. Qiu, C. Liang, P. Song, Y. Han, Y. Han, J. Gu, J. Kong, D. Pan, Z. Guo, Electromagnetic interference shielding MWCNT-Fe3O4@Ag/epoxy nanocomposites with satisfactory thermal conductivity and high thermal stability, Carbon N Y 141 (2019) 506–514, https://doi.org/10.1016/j.carbon.2018.10.003.

[23] C. Fu, C. Yan, L. Ren, X. Zeng, G. Du, R. Sun, J. Xu, C.P. Wong, Improving thermal conductivity through welding boron nitride nanosheets onto silver nanowires via silver nanoparticles, Compos. Sci. Technol. 177 (2019) 118–126, https://doi.org/10.1016/j.compscitech.2019.04.026.

[24] L. Wang, Z. Ma, Y. Zhang, L. Chen, D. Cao, J. Gu, Polymer-based EMI shielding composites with 3D conductive networks: a mini-review, SusMat 1 (2021) 413–431, https://doi.org/10.1002/sus2.21.

[25] R. Turczyn, K. Krukiewicz, A. Katunin, J. Sroka, P. Sul, Fabrication and application of electrically conducting composites for electromagnetic interference shielding of remotely piloted aircraft systems, Compos. Struct. 232 (2020), https://doi.org/10.1016/j.compstruct.2019.111498.

[26] K. Raagulan, R. Braveenth, B.M. Kim, K.J. Lim, S.B. Lee, M. Kim, K.Y. Chai, An effective utilization of MXene and its effect on electromagnetic interference shielding: flexible, free-standing and thermally conductive composite from MXene-PAT-poly(: P-aminophenol)-polyaniline co-polymer, RSC Adv. 10 (2020) 1613–1633, https://doi.org/10.1039/c9ra09522e.

[27] K. Yang, W. Chen, Y. Zhao, L. Ding, B. Du, S. Zhang, W. Yang, Enhancing dielectric strength of thermally conductive epoxy composites by preventing interfacial charge accumulation using micron-sized diamond, Compos. Sci. Technol. 221 (2022), https://doi.org/10.1016/j.compscitech.2021.109178.

[28] Y. Chen, X. Hou, M. Liao, W. Dai, Z. Wang, C. Yan, H. Li, C. Te Lin, N. Jiang, J. Yu, Constructing a "pea-pod-like" alumina-graphene binary architecture for enhancing thermal conductivity of epoxy composite, Chem. Eng. J. 381 (2020), https://doi.org/10.1016/j.cej.2019.122690.

[29] Z. Wang, G. Meng, L. Wang, L. Tian, S. Chen, G. Wu, B. Kong, Y. Cheng, Simultaneously enhanced dielectric properties and through-plane thermal conductivity of epoxy composites with alumina and boron nitride nanosheets, Sci. Rep. 11 (2021), https://doi.org/10.1038/s41598-021-81925-x.

[30] Z. Lule, J. Kim, Thermally conductive and highly rigid polylactic acid (PLA) hybrid composite filled with surface treated alumina/nano-sized aluminum nitride, Compos Part A Appl Sci Manuf 124 (2019), https://doi.org/10.1016/j.compositesa.2019.105506.

[31] C. Xiao, L. Chen, Y. Tang, X. Zhang, K. Zheng, X. Tian, Three dimensional porous alumina network for polymer composites with enhanced thermal conductivity, Compos Part A Appl Sci Manuf 124 (2019), https://doi.org/10.1016/j.compositesa.2019.105511.

[32] N. Song, D. Cao, X. Luo, Q. Wang, P. Ding, L. Shi, Highly thermally conductive polypropylene/graphene composites for thermal management, Compos Part A Appl Sci Manuf 135 (2020), https://doi.org/10.1016/j.compositesa.2020.105912.

[33] H. Guo, H. Zhao, H. Niu, Y. Ren, H. Fang, X. Fang, R. Lv, M. Maqbool, S. Bai, Highly thermally conductive 3D printed graphene filled polymer composites for scalable thermal management applications, ACS Nano 15 (2021) 6917–6928, https://doi.org/10.1021/acsnano.0c10768.

[34] Z.G. Wang, J.C. Lv, Z.L. Zheng, J.G. Du, K. Dai, J. Lei, L. Xu, J.Z. Xu, Z.M. Li, Highly thermally conductive graphene-based thermal interface materials with a bilayer structure for central processing unit cooling, ACS Appl. Mater. Interfaces (2021), https://doi.org/10.1021/acsami.1c01223.

[35] H. Yu, P. Guo, M. Qin, G. Han, L. Chen, Y. Feng, W. Feng, Highly thermally conductive polymer composite enhanced by two-level adjustable boron nitride network with leaf venation structure, Compos. Sci. Technol. 222 (2022), https://doi.org/10.1016/j.compscitech.2022.109406.

[36] V. Guerra, C. Wan, T. McNally, Thermal conductivity of 2D nano-structured boron nitride (BN) and its composites with polymers, Prog. Mater. Sci. 100 (2019) 170–186, https://doi.org/10.1016/j.pmatsci.2018.10.002.

[37] X. Chen, J.S.K. Lim, W. Yan, F. Guo, Y.N. Liang, H. Chen, A. Lambourne, X. Hu, Salt template assisted BN scaffold fabrication toward highly thermally conductive epoxy composites, ACS Appl. Mater. Interfaces 12 (2020) 16987–16996, https://doi.org/10.1021/acsami.0c04882.

[38] Z. Liu, J. Li, X. Liu, Novel functionalized BN nanosheets/epoxy composites with advanced thermal conductivity and mechanical properties, ACS Appl. Mater. Interfaces 12 (2020) 6503–6515, https://doi.org/10.1021/acsami.9b21467.

[39] Y. Cui, D. Bao, F. Xu, Y. Gao, X. Zhang, H. Geng, Y. Zhou, Y. Zhu, H. Wang, Fabrication of EVA connected 3D BN network for enhancing the thermal conductivity of epoxy composites, Compos. B Eng. 224 (2021), https://doi.org/10.1016/j.compositesb.2021.109203.

[40] H. Yu, Y. Feng, C. Chen, Z. Zhang, Y. Cai, M. Qin, W. Feng, Thermally conductive, self-healing, and elastic Polyimide@Vertically aligned carbon nanotubes composite as smart thermal interface material, Carbon N Y 179 (2021) 348–357, https://doi.org/10.1016/j.carbon.2021.04.055.

[41] R. Cong, C. Xu, Y. Chen, F. Ran, G. Fang, Enhanced thermal conductivity of palmitic acid/copper foam composites with carbon nanotube as thermal energy storage materials, J. Energy Storage 40 (2021), https://doi.org/10.1016/j.est.2021.102783.

[42] B. Shin, S. Mondal, M. Lee, S. Kim, Y. Il Huh, C. Nah, Flexible thermoplastic polyurethane-carbon nanotube composites for electromagnetic interference shielding and thermal management, Chem. Eng. J. 418 (2021), https://doi.org/10.1016/j.cej.2021.129282.

[43] W. Lee, J. Kim, Enhanced through-plane thermal conductivity of paper-like cellulose film with treated hybrid fillers comprising boron nitride and aluminum nitride, Compos. Sci. Technol. 200 (2020), https://doi.org/10.1016/j.compscitech.2020.108424.

[44] S. Lee, D. Park, J. Kim, 3D-printed surface-modified aluminum nitride reinforced thermally conductive composites with enhanced thermal conductivity and

mechanical strength, Polym. Adv. Technol. 33 (2022) 1291–1297, https://doi.org/10.1002/pat.5601.
[45] L. Qiu, K. Yan, Y. Feng, X. Liu, X. Zhang, Bionic hierarchical porous aluminum nitride ceramic composite phase change material with excellent heat transfer and storage performance, Compos. Commun. 27 (2021), https://doi.org/10.1016/j.coco.2021.100892.
[46] M. Ma, L. Xu, L. Qiao, S. Chen, Y. Shi, H. He, X. Wang, Nanofibrillated Cellulose/MgO@rGO composite films with highly anisotropic thermal conductivity and electrical insulation, Chem. Eng. J. 392 (2020), https://doi.org/10.1016/j.cej.2019.123714.
[47] X. Zhou, C. Ding, C. Cheng, S. Liu, G. Duan, W. Xu, K. Liu, H. Hou, Mechanical and thermal properties of electrospun polyimide/rGO composite nanofibers via in-situ polymerization and in-situ thermal conversion, Eur. Polym. J. 141 (2020), https://doi.org/10.1016/j.eurpolymj.2020.110083.
[48] H. Lin, M. Ma, Q. Chu, L. Xu, S. Chen, Y. Shi, H. He, X. Wang, Multifunctional nanofibrillated cellulose/ZnO@rGO composite films for thermal conductivity, electrical insulation, and antibacterial applications, Compos. Struct. 312 (2023), https://doi.org/10.1016/j.compstruct.2023.116896.
[49] Q. Hu, X. Bai, C. Zhang, X. Zeng, Z. Huang, J. Li, J. Li, Y. Zhang, Oriented BN/Silicone rubber composite thermal interface materials with high out-of-plane thermal conductivity and flexibility, Compos Part A Appl Sci Manuf 152 (2022), https://doi.org/10.1016/j.compositesa.2021.106681.
[50] Y. Zhang, X. Tai, J. Zhou, T. Zhai, L. Xu, C. Diao, X. Xie, C. Hou, X. Sun, X. Zhang, Z. Li, W. Du, Enhanced high-temperature thermal conductivity of the reduced graphene oxide@SiO2 composites synthesised by liquid phase deposition, Ceram. Int. 48 (2022) 8481–8488, https://doi.org/10.1016/j.ceramint.2021.12.058.
[51] K. Chen, X. Tang, B. Jia, C. Chao, Y. Wei, J. Hou, L. Dong, X. Deng, T.H. Xiao, K. Goda, L. Guo, Graphene oxide bulk material reinforced by heterophase platelets with multiscale interface crosslinking, Nat. Mater. 21 (2022) 1121–1129, https://doi.org/10.1038/s41563-022-01292-4.
[52] L. Liu, M. Zhu, Z. Ma, X. Xu, S. Mohesen Seraji, B. Yu, Z. Sun, H. Wang, P. Song, A reactive copper-organophosphate-MXene heterostructure enabled antibacterial, self-extinguishing and mechanically robust polymer nanocomposites, Chem. Eng. J. 430 (2022), https://doi.org/10.1016/j.cej.2021.132712.
[53] J. Cho, P.C. Su, J. Kim, Highly thermally conductive and insulating composites fabricated through the hot-pressing of hollow structured h-BN/rGO hybrid filler, Appl. Mater. Today 37 (2024), https://doi.org/10.1016/j.apmt.2024.102149.
[54] D.S. Muratov, V. Vanyushin, V.A. Koshlakova, E.A. Kolesnikov, A.V. Maksimkin, A. A. Stepashkin, D.V. Kuznetsov, Improved mechanical and thermal properties of polypropylene filled with reduced graphene oxide (rGO) and hexagonal boron nitride (hBN) particles, J. Alloys Compd. 972 (2024), https://doi.org/10.1016/j.jallcom.2023.172882.
[55] J. Hong, N. Luo, Z. Zhang, L. Zhang, G. Zhang, L. Ye, S.S. Ray, Y. Li, Regulated orientation and exfoliation of flaky fillers by close packing structures in polymer composites for excellent thermal conduction and EMI shielding, Compos. B Eng. 275 (2024), https://doi.org/10.1016/j.compositesb.2024.111357.
[56] L. Zhang, H. Liu, Z. Wang, W. Sui, Y. Gong, J. Cui, Y. Ao, L. Shang, Functional boron nitride/graphene oxide three-dimensional skeleton co-heat transfer epoxy resin composite, J. Alloys Compd. 985 (2024), https://doi.org/10.1016/j.jallcom.2024.173935.
[57] R. Li, T. Gao, Y. Wang, Y. Chen, W. Luo, Y. Wu, Y. Xie, Y. Wang, Y. Zhang, Engineering of bimetallic Au–Pd alloyed particles on nitrogen defects riched g-C3N4 for efficient photocatalytic hydrogen production, Int. J. Hydrogen Energy 63 (2024) 1116–1127, https://doi.org/10.1016/j.ijhydene.2024.03.113.
[58] Y. Wang, T. Gao, R. Li, Y. Chen, W. Luo, Y. Wu, Y. Xie, Y. Wang, Y. Zhang, Layered deposited MoS2 nanosheets on acorn leaf like CdS as an efficient anti-photocorrosion photocatalyst for hydrogen production, Fuel 368 (2024), https://doi.org/10.1016/j.fuel.2024.131621.
[59] W. Tang, H. Ye, Y. Xie, P. Chen, L. Luo, Y. Zhang, Transition metal bismuth spheres dispersed and anchored in benzene-ring-grafted porous g-C3N4 nanosheets for photocatalytic reduction of CO2, Chem. Eng. J. 478 (2023), https://doi.org/10.1016/j.cej.2023.147350.
[60] F. Zhou, J. Zhang, Y. Zhang, Y. Wu, Y. Wang, W. Luo, Palladium-Copper bimetallic catalysts for electroreduction of CO2 and nitrogenous species, Coord. Chem. Rev. 509 (2024), https://doi.org/10.1016/j.ccr.2024.215802.
[61] P. Choudhary, K. Kumari, D. Sharma, S. Kumar, V. Krishnan, Surface nanoarchitectonics of boron nitride nanosheets for highly efficient and sustainable ipso-hydroxylation of arylboronic acids, ACS Appl. Mater. Interfaces (2022), https://doi.org/10.1021/acsami.2c21545.
[62] S.C. Karthikeyan, R. Santhosh Kumar, S. Ramakrishnan, S. Prabhakaran, A.R. Kim, D.H. Kim, D.J. Yoo, Efficient alkaline water/seawater electrolysis by development of ultra-low IrO2Nanoparticles decorated on hierarchical MnO2/rGO nanostructure, ACS Sustain Chem Eng 10 (2022) 15068–15081, https://doi.org/10.1021/acssuschemeng.2c04074.
[63] N. Duan, Z. Shi, J. Wang, X. Zhang, C. Zhang, C. Zhang, G. Wang, Multilayer-structured carbon fiber fabric/graphene oxide/Fe3O4/epoxy composite for highly efficient mechanical and electromagnetic interference shielding, Appl. Surf. Sci. 613 (2023), https://doi.org/10.1016/j.apsusc.2022.156038.